Prostate Segmentation: An Efficient Convex Optimization Approach With Axial Symmetry Using 3-D TRUS and MR Images

Wu Qiu*, *Member, IEEE*, Jing Yuan, *Member, IEEE*, Eranga Ukwatta, *Student Member, IEEE*, Yue Sun, Martin Rajchl, *Student Member, IEEE*, and Aaron Fenster, *Fellow, IEEE*

Abstract—We propose a novel global optimization-based approach to segmentation of 3-D prostate transrectal ultrasound (TRUS) and T2 weighted magnetic resonance (MR) images, enforcing inherent axial symmetry of prostate shapes to simultaneously adjust a series of 2-D slice-wise segmentations in a "global" 3-D sense. We show that the introduced challenging combinatorial optimization problem can be solved globally and exactly by means of convex relaxation. In this regard, we propose a novel *coherent continuous max-flow model* (CCMFM), which derives a new and efficient duality-based algorithm, leading to a GPU-based implementation to achieve high computational speeds. Experiments with 25 3-D TRUS images and 30 3-D T2w MR images from our dataset, and 50 3-D T2w MR images from a public dataset, demonstrate that the proposed approach can segment a 3-D prostate TRUS/MR image within 5–6 s including 4–5 s for initialization, yielding a mean Dice similarity coefficient of $93.2\% \pm 2.0\%$ for 3-D TRUS images and $88.5\% \pm 3.5\%$ for 3-D MR images. The proposed method also yields relatively low intra- and inter-observer variability introduced by user manual initialization, suggesting a high reproducibility, independent of observers.

Index Terms—Convex optimization, rotational symmetry, three-dimensional (3-D) prostate magnetic resonance imaging (MRI), three-dimensional (3-D) prostate transrectal ultrasound (TRUS).

I. INTRODUCTION

RECENT development of prostate biopsy systems based on fusing 3-D transrectal ultrasound (TRUS) images with magnetic resonance (MR) images [1], [2] has demonstrated increased positive yield and greater number of cores with higher Gleason grade [3]. This technique provides an alternative to magnetic resonance imaging (MRI)-based prostate biopsy [4] to indirectly target biopsy needles toward regions of the prostate containing suspicious lesions identified with MR imaging, by means of 3-D TRUS-MRI registration [5]. Thus, an efficient and accurate prostate segmentation method for both 3-D MR and TRUS images is highly desired for the surface-based MR to 3-D TRUS registration [6], [7]. In addition, prostate segmentation from 3-D TRUS and MRI plays a key role in clinical decision making process. For instance, segmented prostate volume can be used to assist to diagnose the benign prostate hyperplasia [8]. Identification of the prostate surface can also be utilized in different treatments of prostate diseases, such as prostate brachytherapy [9], [10], high intensity focused ultrasonography (HIFU) [11], cryotherapy [12], minimally invasive ablative, and external beam radiation therapy [13], [14]. Other imaging modality guided prostate biopsy systems can also benefit from this technique, such as PET/CT directed 3-D TRUS guided prostate biopsy system [15]. Considering the arduous and timeconsuming effort associated with manual 3-D prostate segmentation, an accurate and efficient automated or semi-automated 3-D prostate segmentation would be highly beneficial. However, the presence of US speckle, shadowing due to calcifications, missing edges or texture similarities between the inner and outer regions of the prostate in TRUS images [16], and widely distributed high-contrast edges and intensity inhomogeneities in MR images make it challenging to implement such an automated or semi-automated segmentation for both image modalities.

Even though there are extensive studies [17]–[23] in delineating prostate boundaries from both 3-D TRUS and MR images, most of previous studies rely on classifiers, atlas or deformable models, which usually cannot meet the requirements for both efficiency and accuracy for clinical routine use. For more details of existing methods refer to [24]–[26]. To the best of our knowledge, there is no report on prostate segmentation method working well for both TRUS and MR images. Therefore, a more efficient and accurate 3-D prostate segmentation for 3-D TRUS/MR images is still needed in practice, especially in fused 3-D TRUS/MR image guided prostate biopsy systems. To achieve this goal, additional information about prostate shapes can be used to greatly help to guide locating the correct prostate boundaries, where such shape priors can be either learned through the specified training data set [27], [28] or directly modeled in a geometrically compact way [29]. However, in addition to the extra computation cost to the introduced shape learning or modeling description, the wide variety of prostate shape appearances often makes the shape learning step a computationally intensive task for a precise
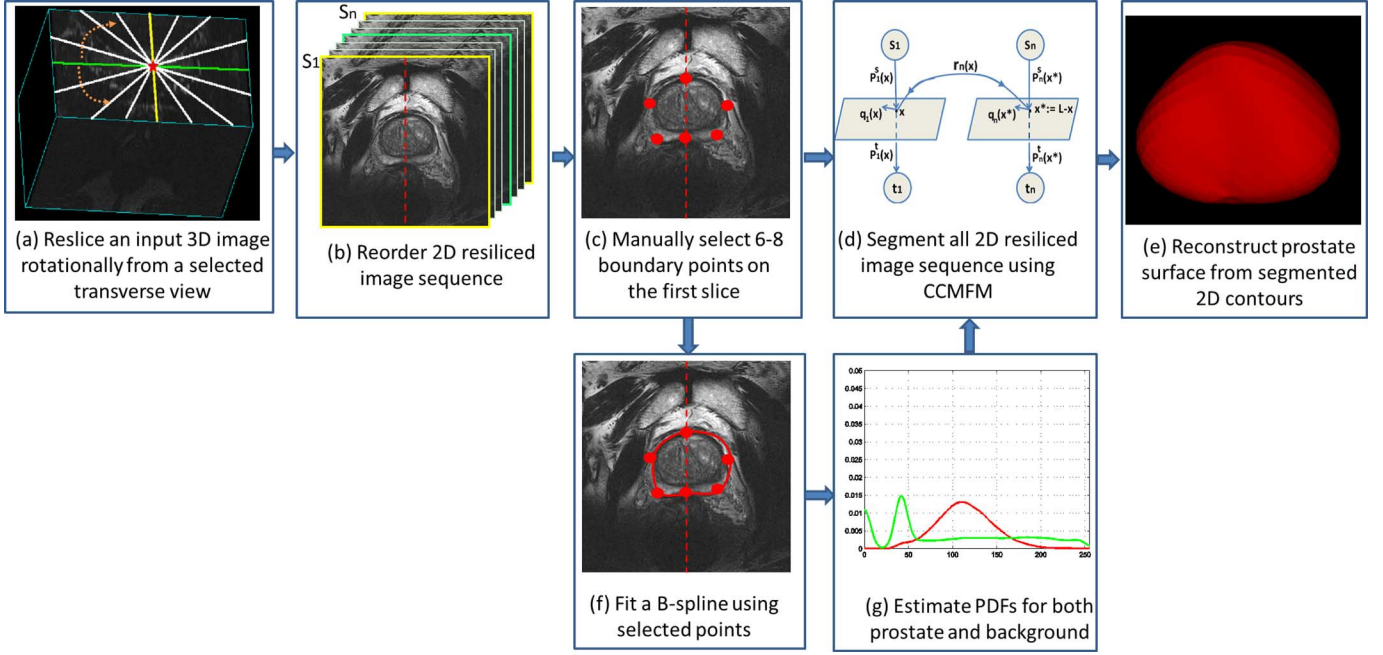
Fig. 1.   Block diagram of the segmentation pipeline.

shape description, especially for 3-D prostate shapes. Additionally, exploring variations of prostate shapes and sizes across different patient studies also requires additional procedure to introduce the shape information properly for a correct prostate segmentation.

In this study, we employ an inherent *geometric/axial symmetry* as the shape prior to 3-D prostate segmentation for both TRUS and MR modality images and propose a new and efficient global optimization based approach to the derived segmentation problem. More specifically, an input 3-D prostate image is first resliced rotationally along a specified axis into a sequence of 2-D slices, the proposed method segments these 2-D slices simultaneously while globally enforcing the spatial coherence of the prostate regions within every two adjacent slices. We also show that the introduced challenging combinatorial optimization problem can be globally optimized by means of convex relaxation. Moreover, we introduce a novel *coherent continuous max-flow model* (CCMFM), which is dual/equivalent to the formulated convex relaxed optimization problem. With help of the new CCMFM, we can prove that the proposed combinatorial optimization problem can be solved globally and exactly, i.e., the globally optimal segmentation of the n 2-D slices with respect to such *axial symmetry prior* can be accordingly achieved. We derive a new and efficient multiplier augmented algorithm based on the CCMFM, which avoids directly tackling the original nonsmooth convex energy functional and can be readily implemented on a GPU to achieve a substantial speed-up in computation.

In fact, utilizing the axial symmetry of the prostate has been introduced to the segmentation of 3-D prostate TRUS images [30]–[32], for which the segmentation of one 2-D slice is propagated to assist segmenting its succeeding slice. However, such propagation procedures often carry segmentation errors appearing in one slice to the segmentation of its following slices, thus causing an accumulated segmentation errors in all subsequent segmentations. In addition, the segmentation result of any slice does not help in refining the segmentation of its preceding slices. Furthermore, sequentially segmenting 2-D slices by the active contour [30] or level-set [31], [32] is numerically not efficient and can often be trapped by a local optimum. In contrast, the proposed approach introduced in this paper avoids these disadvantages by jointly optimizing the segmentations of all the slices under a "global" perspective. A preliminary study of this work has been previously described in CVPR conference [33], which was only validated on a small number of 3-D TRUS images. More details on the algorithm and its implementation are provided in this paper. The proposed algorithm is also comprehensively validated in terms of accuracy, efficiency, parameter sensitivity, both intra- observer and inter-observer variability with a larger number of 3-D TRUS and T2w MR prostate images than the preliminary study.

II. METHOD

A. Segmentation Overview

The proposed 3-D prostate segmentation method is divided into five steps.

1) Let $\mathcal{V}$ be an input 3-D prostate TRUS/MR image, which is rotationally resliced in both clockwise and counter clockwise directions of 90° [orange dotted arrows in Fig. 1(a)] along a given axis [red star in Fig. 1(a) and red dash-line in Fig. 1(b), (c), and (f)] to n 2-D images $\mathcal{S}_1 \ldots \mathcal{S}_n$ [white lines in Fig. 1(a)]. The essential shape of prostate allows the specification of the rotational axis, such that prostate regions on every two adjacent slices are spatially consistent, namely an *axial symmetry prior*. It should be noted that reslicing a 3-D cube in two directions leads to left-right flipping of the horizontal coordi-
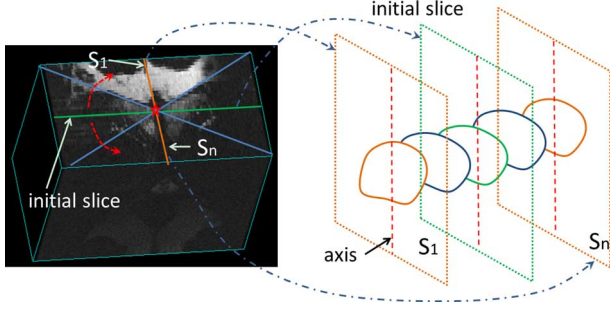
Fig. 2. Schematic diagram of stacking all 2-D resliced images.
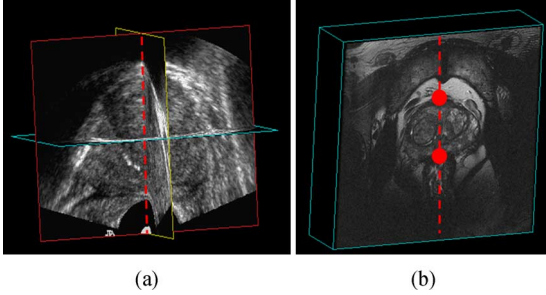

(a)   (b)

Fig. 3. Examples of the selection of the rotational axis from transverse views in (a) TRUS and (b) MR images.

nates of the last slice compared to horizontal coordinates of the first slice, as shown in Fig. 2 and Fig. 4(a).

Typically, we manually sliced into the 3-D image from the transverse view of the prostate to locate the initial resliced image [green slices in Fig. 1(a) and (b)], where the prostate has the largest area in 2-D views. In 3-D TRUS images, we use the 3-D scanning axis as the rotational axis, which is in the middle of the 2-D ultrasound image generated by the TRUS probe. All the 2-D images intersect along the 3-D scanning axis and have an equal angular spacing, as shown in Fig. 3(a). In 3-D MR images, after the first resliced image is determined, the rotational axis needs to be selected manually by identifying two points on the approximated symmetrical axis of the prostate from the transverse view, as shown in Fig. 3(b).

2) All resliced 2-D images are reoriented and stacked into a new 3-D cube by aligning the rotational axis [Fig. 1(b)]. Thus, all stacked prostate contours appear as an approximated tubular structure, as shown in Fig. 2.

3) Six to eight initialization points (red points) are manually chosen from the prostate boundary in the initial slice [Fig. 1(c)], in which the initial prostate contour is estimated using a cardinal spline interpolation [Fig. 1(f)]. The voxels inside the fitted contour are marked as the prostate voxels, which are used to estimate the intensity probability distribution function (PDF) model for the prostate [Fig. 1(g)]. The voxels in the region outside the fitted contour by a distance of 50–100 voxels are sampled as the background voxels that are used to estimate the intensity PDF for the background. In our experiments, the sampled background voxels are fixed

to be in their corresponding region as hard constraints of the segmentation regions.

4) All 2-D resliced image sequences are simultaneously segmented using the proposed CCMFM [Fig. 1(d)].

5) A 3-D prostate surface is then reconstructed from the segmented contours in all 2-D slices [Fig. 1(e)].

B. Optimization Formulation With Axial Symmetry Prior

In this section, we propose a novel and efficient global optimization approach to simultaneously extract n prostate contours of the slices $\mathcal{S}_1 \dots \mathcal{S}_n$ by jointly enforcing their *axial symmetry prior*. We show that the proposed combinatorial optimization problem can be exactly and globally solved by convex relaxation. In this regard, we introduce a new spatially continuous max-flow model, which is dual/equivalent to the convex relaxed optimization formulation and provides great advantages in both mathematical analysis and algorithm design. Let $\mathcal{R}_i$, $i = 1 \dots n$, denote the prostate region of the 2-D slice $\mathcal{S}_i$, and $u_i(x)$, $i = 1 \dots n$, be the labeling function of the prostate region $\mathcal{R}_i$ such that

$$u_i(x) = \begin{cases} 1, & \text{for } \forall x \in \mathcal{R}_i \\ 0, & \text{otherwise} \end{cases}, \quad i = 1 \dots n.$$

The segmentation of each slice $\mathcal{S}_i$, $i = 1 \dots n$, can be formulated as the spatially continuous min-cut problem [34], [35] as follows:

$$\min_{u_i(x) \in \{0,1\}} E_i(u_i)$$
$$:= \langle 1 - u_i, C_i^s \rangle + \langle u_i, C_i^t \rangle + \int_\Omega g_i(x) |\nabla u_i| \, dx \quad (1)$$

Ω is denoted as image space, and we define two cost functions $C_i^s(x)$ and $C_i^t(x)$ to label each pixel $x \in \mathcal{S}_i$ as: $C_i^s(x) := -\log \phi_{fg}(x)$ and $C_i^t(x) = -\log \phi_{bg}(x)$, $i = 1 \dots n$, where $\phi_{fg}(x)$ and $\phi_{bg}(x)$ are the intensity PDFs with respect to the prostate region and background, respectively, estimated by sampled pixels in the first slice. Moreover, the weighted total-variation function of (1) measures the minimum geodesic length indicated by the labeling function $u_i(x) \in \{0,1\}$, $i = 1 \dots n$, and it is positive and given by

$$g_i(x) = \lambda_1 + \lambda_2 \exp(-\lambda_3 |\nabla \mathcal{S}_i(x)|), \quad \lambda_{1,2,3} \geq 0. \quad (2)$$

Note that, the values of $g_i(x)$ fall within the range $[\lambda_1, \lambda_1 + \lambda_2]$..

In this work, the n slices $\mathcal{S}_1 \dots \mathcal{S}_n$ are simply aligned along the specified rotational axis, such that the rotational axis vertically bisects the prostate [see the red dotted line in Fig. 1(c) and (f)]. We enforce the *axial symmetry prior* of the prostate by penalizing the spatial inconsistency of the extracted regions within two neighbor slices, i.e., the area difference of the two adjacent prostate regions is penalized as

$$\pi_i(u) := \int_\Omega |u_{i+1} - u_i| \, dx, \quad i = 1 \dots n - 1 \quad (3)$$

and the area difference of $\mathcal{R}_n$ and $\mathcal{R}_1$ within the last and first slices

$$\pi_n(u) := \int_\Omega |u_n(L - x_1, x_2) - u_1(x_1, x_2)| \, dx \quad (4)$$
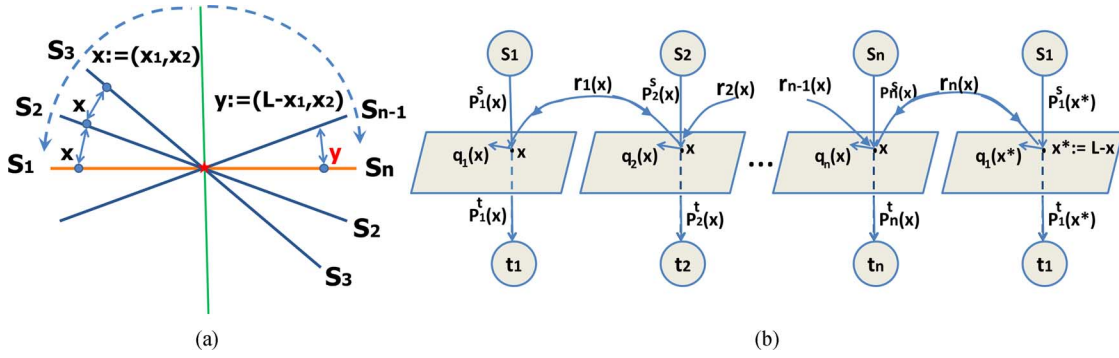
Fig. 4. Flow-maximization configurations: (a) shows the flow-maximization configuration between two adjacent slices; (b) shows the flow-maximization configuration between the last and first slices.

where $x := (x_1, x_2)$ and the spatial comparison is performed by left-right flipping horizontal coordinates of the last slice, as shown in Fig. 2 and Fig. 4(a), and L is defined as the horizontal coordinate x_1 of the rotational axis.

We extract the 3-D prostate surface of the input 3-D image by means of indirectly segmenting all the resliced n 2-D slices while incorporating their *axial symmetry prior*. In view of (1), (3) and (4), it can be formulated as follows:

$$\min_{\mathbf{u}_{1\ldots n}(\mathbf{x}) \in \{0,1\}} \sum_{k=1}^{n} E_i(u_i) + \alpha \sum_{k=1}^{n} \pi_i(u). \quad (5)$$

C. Convex Relaxation and Coupled Continuous Max-Flow Model

In this work, we can demonstrate that the proposed optimization problem (5) can be globally and exactly solved by its convex relaxation

$$\min_{\mathbf{u}_{1\ldots n}(\mathbf{x}) \in [0,1]} \sum_{k=1}^{n} E_i(u_i) + \alpha \sum_{k=1}^{n} \pi_i(u) \quad (6)$$

where the binary-valued constraints $u_{1\ldots n}(x) \in \{0,1\}$ in (5) is replaced by its convex relaxation $u_{1\ldots n}(x) \in [0,1]$. We investigate the convex optimization problem (6) under the primal and dual perspective, for which we introduce a novel CCMFM and demonstrate that it is dual or equivalent to (6). With help of the introduced CCMFM, we prove that the computed global optimum of the convex relaxation problem (6) can also be used to solve its original combinatorial optimization problem (5) globally and exactly. In addition, the CCMFM derives a new and efficient algorithm to (6) without directly tackling its nonsmooth function terms, i.e., the total variation functions and the L_1-norm functions in (6).

We first introduce the new spatially continuous configuration of flows [as illustrated in Fig. 4(a) and (b)], such as follows.

- For each image slice $\mathcal{S}_i$, $i = 1 \ldots n$, two additional flow terminals: the source s_i and the sink t_i, are added. We link the source s_i to each pixel x in $\mathcal{S}_i$ and there is a flow $p_i^s(x)$ streaming from s_i to x. We also link each pixel $x \in \mathcal{S}_k$ to the sink t_i and there is a flow $p_k^t(x)$ streaming from x to t_i; within $\mathcal{S}_i$, there is a local vector flow field $q_i(x) \in \mathbb{R}^2$ around x.

- Between two adjacent slices $\mathcal{S}_i$ and $\mathcal{S}_{i+1}$, $i = 1 \ldots n-1$, we link $x \in \mathcal{S}_i$ to the same pixel $x \in \mathcal{S}_{i+1}$ and there is a flow $r_i(x)$ streaming in both directions. Between the last slice $\mathcal{S}_n$ and the first slice $\mathcal{S}_1$, we link the pixel $x := (x_1, x_2) \in \mathcal{S}_1$ to the pixel $(L - x_1, x_2) \in \mathcal{S}_n$ and there is a flow $r_n(x)$ streaming in both directions.

With the above flow settings, we formulate the new CCMFM by maximizing the total amount of flows streaming from the n sources $s_1 \ldots s_n$, such that

$$\max_{p^s, p^t, q, r} \sum_{k=1}^{n} \int_{\Omega} p_k^s(x) \, dx \quad (7)$$

subject to the following flow constraints.
- *Capacity constraints on source and sink flows:*

$$p_i^s(x) \le C_i^s(x), \ p_i^t(x) \le C_i^t(x); \ i = 1 \ldots n. \quad (8)$$

- *Capacity constraints on spatial flows:*

$$|q_i(x)| \le g_i(x), \ i = 1 \ldots n. \quad (9)$$

- *Capacity constraints on coupled flows:*

$$|r_i(x)| \le \alpha, \ i = 1 \ldots n. \quad (10)$$

- *Flow conservation constraints:* all the flows at each pixel of every slice are balanced, i.e., for each of the last $n-1$ slices $\mathcal{S}_i$, $i = 2 \ldots n$, at each position $x \in \mathcal{S}_i$, it must suffice

$$\rho_i(x) := \big(\operatorname{div} q_i - p_i^s + p_i^t + r_i - r_{i-1}\big)(x) = 0 \quad (11)$$

and for the first slice $\mathcal{S}_1$, at each position $x := (x_1, x_2) \in \mathcal{S}_1$, the total flow balance is evaluated by

$$\rho_1(x) := \big(\operatorname{div} q_1 - p_1^s + p_1^t + r_1\big)(x) - r_n(L - x_1, x_2) = 0. \quad (12)$$

By introducing the multiplier functions $u_i(x)$, $i = 1 \ldots n$, to the linear equalities (12) and (11) with respect to the flow conservation conditions, we then have the equivalent primal-dual model of (7) as follows:

$$\min_{u_1 \ldots u_n} \max_{p^s, p^t, q, r} \sum_{i=1}^{n} \int_{\Omega} p_i^s(x) \, dx + \sum_{i=1}^{n} \langle u_i, \rho_i \rangle \quad (13)$$

subject to the flow capacity constraints (8)–(10).

Through variational analysis, we can prove the following dualities:

Proposition 1: The proposed CCMFM (7) *is dual or equivalent to the convex relaxation problem* (6), *and also the primal-dual model* (13), *i.e.,*

$$(7) \iff (6) \iff (13). \quad (14)$$

Moreover, with help of the CCMFM (7), we have:

Proposition 2: Let $(u_1^*(x), \ldots u_n^*(x)) \in [0, 1]$ *be the global optimum of the convex relaxation problem* (6), *the thresholdings* $u_i^\gamma(x) \in \{0, 1\}$, $i = 1 \ldots n$, *by any* $\gamma \in [0, 1)$, *where*

$$u_i^\gamma(x) = \begin{cases} 1, & \text{when } u_k^*(x) > \gamma \\ 0, & \text{when } u_k^*(x) \leq \gamma \end{cases}, \quad i = 1 \ldots n \quad (15)$$

solves the original combinatorial optimization problem (5) *globally and exactly.*

The proofs to Prop. 1 and Prop. 2 are given in the Appendix.

D. Coherent Continuous Max-Flow Algorithm

Through Prop. 2, we see that the global optimum of the challenging combinatorial optimization problem (5) can be achieved by thresholding the optimum of its convex relaxation (6) with any parameter $\gamma \in [0, 1)$. Furthermore, in view of Prop. 1, it is also easy to see that the optimum of such convex relaxation problem (6) is just given by the optimal multipliers to the corresponding flow conservation conditions (11) and (12). Indeed, this allows to directly derive the *coupled continuous max-flow algorithm* based on the CCMFM (7) and the modern augmented Lagrangian algorithm [36], [37], which computes both the maximum total flows from the n sources and the optimum continuous labeling functions $u_{1 \ldots n}(x) \in [0, 1]$. Especially, we will see the new *coupled continuous max-flow algorithm* is efficient and successfully avoids directly tackling the nonsmooth function terms of (6).

In view of (13), we define the augmented Lagrangian function as follows:

$$L_c(u, p^{s,t}, q, r) := \sum_{i=1}^{n} \left\{ \int_\Omega p_i^s(x)\, dx + \langle u_i, \rho_i \rangle - \frac{c}{2} \|\rho_i\|^2 \right\}$$

where $c > 0$ is constant. By means of the augmented Lagrangian algorithm, we propose the *coupled continuous max-flow algorithm* such that, at each kth iteration.

1) Maximize $L_c(u, p^{s,t}, q, r)$ over the spatial flows $|q_i(x)| \leq g(x)$, $i = 1 \ldots n$, while fixing the other variables $(u, p^{s,t}, r)^k$, which amounts to

$$q_i^{k+1} := \arg\max_{|q_i(x)| \leq g(x)} -\frac{c}{2} \|\text{div } q_i - F_i^k\|^2$$

where $F_i^k(x)$ is fixed. This can be computed by the gradient-projection iteration

$$q_i^{k+1} = \text{Proj}_{|q_i(x)| \leq g(x)} (q_i^k + \tau \nabla(\text{div } q_i^k - (F_i^k))) \quad (16)$$

where $\tau > 0$ is some step-size for convergence [38].

2) Maximize $L_c(u, p^{s,t}, q, r)$ over the source flows $p_i^s(x) \leq C_i^s(x)$, $i = 1 \ldots n$, while fixing the other variables $(u, p^t, q, r)^k$, which amounts to

$$(p_i^s)^{k+1} := \arg\max_{p_i^s(x) \leq C_i^s(x)} \int_\Omega p_i^s\, dx - \frac{c}{2} \|p_i^s - G_i^k\|^2$$

where $G_i^k(x)$ is fixed. This can be solved exactly by

$$(p_i^s)^{k+1}(x) = \min\left(G_i^k(x) + \frac{1}{c}, C_i^s(x) \right). \quad (17)$$

3) Maximize $L_c(u, p^{s,t}, q, r)$ over $p_i^t(x) \leq C_i^t(x)$, $i = 1 \ldots n$, while fixing the other variables $(u, p^s, q, r)^k$, which amounts to

$$(p_i^t)^{k+1} := \arg\max_{p_i^t(x) \leq C_i^t(x)} -\frac{c}{2} \|p_i^t - H_i^k\|^2$$

where $H_1^k(x)$ is fixed. This can be solved exactly by

$$(p_i^t)^{k+1}(x) = \min(H_i^k(x), C_i^t(x)). \quad (18)$$

4) Maximize $L_c(u_{1,2}, p_s^{1,2}, p_t^{1,2}, q_{1,2}, r)$ over the coupled flow field $|r(x)| \leq \beta$ by fixing $(q_{1,2}, p_s^{1,2}, p_t^{1,2})^{k+1}$ and $(u_{1,2})^k$, which gives

$$r^{k+1} := \arg\max_{|r(x)| \leq \beta} -\frac{c}{2} \|r + J_1^k\|^2 - \frac{c}{2} \|r - J_2^k\|^2$$

where $J_1^k = \text{div } q_1^{k+1} - (p_s^1)^{k+1} + (p_t^1)^{k+1} - (u_1)^k/c$ and $J_2^k = \text{div } q_2^{k+1} - (p_s^2)^{k+1} + (p_t^2)^{k+1} - (u_2)^k/c$. It can be computed exactly by

$$r^{k+1} = \frac{(J_2 - J_1)}{2}.$$

5) Update the labeling functions $u_i^{k+1}(x)$, $i = 1 \ldots n$, by

$$u_1^{k+1}(x) = u_i^k(x) - c\,\rho_i^{k+1}(x). \quad (19)$$

Let $k = k + 1$ and repeat the above steps until convergence is achieved.

In practice, the experiments show only one gradient-projection iteration (16) is needed to achieve convergence, which greatly improves numerical efficiency.

III. EXPERIMENTS

A. Image Acquisitions

The proposed approach was validated in two datasets including an in-house dataset acquired in our laboratory comprising of 25 3-D prostate TRUS and 30 3-D T2w MR images, and a public 3-D MR image dataset provided by 2012 MICCAI challenge [39]. All subjects involved in image acquisitions in our collaborating hospital provided written informed consent, which was approved by the Research Ethics Board at the University of Western Ontario, London, ON, Canada. All subjects were suspected to have tumors identified by multi-spectral MR imaging.

1) 3-D TRUS Images: 25 3-D TRUS prostate images used for testing were acquired with a rotational scanning 3-D TRUS imaging system, developed for 3-D TRUS guided prostate biopsy [40], and using a commercially available end-firing 5–9 MHz TRUS transducer (Philips Medical Systems, Seattle, WA, USA). The size of each 3-D image was $448 \times 448 \times 350$ voxels of size $0.19 \times 0.19 \times 0.19$ mm^3. It should be noted that the proposed method was only applied on 3-D TRUS images with a complete prostate after the 3-D acquisition was performed. This is ensured by first adjusting the ultrasound depth setting after general exploration of the prostate using 2-D TRUS imaging.

2) 3-D T2w MR Images: The proposed algorithm was also evaluated on 30 3-D T2w MR images from a dataset obtained in our institution. All subjects were scanned at 3.0T with GE Excite HD MRI systems (Milwaukee, WI, USA). 15 images were acquired with a phased-array body coil at a size of $512 \times 512 \times 36$ voxels with a voxel size of $0.27 \times 0.27 \times 2.2$ mm^3, and the other 15 were acquired using a disposable endo-rectal coil (BPX30, MEDRAD, INC) with the same voxel size.

3) Public Dataset: There are a few publicly available datasets of prostate images, such as 2012 MICCAI challenge (PROMISE12) [39] and NCI-ISBI 2013 Challenge [41]. We just validated our algorithm on the dataset from 2012 MICCAI challenge, which is a representative set of the types of MR images acquired in a clinical setting. The data comprising of the 30 cases is multi-center and multi-vendor and has different acquisition protocols (i.e., differences in slice thickness, with/without endorectal coil). For each case in this dataset, a 3-D T2w MR transverse image of the prostate was included in addition to a reference segmentation.

B. Evaluation Metrics

Our segmentation method was evaluated by comparing the algorithm to manual segmentation results using Dice similarity coefficient (DSC) [42], the mean absolute surface distance (MAD) and maximum absolute surface distance (MAXD) [11], and volume difference (VD) [43]. Each prostate image was divided into three subregions, base, mid-gland and apex, according to the apex-base axis of the manual segmented prostate surface (respectively, 0.3, 0.4, 0.3 length fraction of the base-apex axis) [18]. Since the proposed method needs user initialization introducing observer variability, 10 3-D TRUS prostate images were randomly selected to assess the inter- and intra-observer variability of the proposed approach for 3-D TRUS images. In addition, 15 3-D MR images including five endocoil MR images and five bodycoil MR images from our dataset, and five images from public dataset, were randomly selected to evaluate the observer variability of the proposed algorithm for 3-D MR images. Each image was segmented five times by the first observer for assessing the intra-observer variability. The mean run time of five repeated segmentations for each volume was considered as the segmentation time used to evaluate the algorithm efficiency. All selected images were also segmented by three other observers for evaluating the inter-observer variability. The coefficient of variation (CV) [44] of DSC was used as the metric for assessing the intra- and inter-observer variability of our method.

TABLE I
ALGORITHM PARAMETERS VALUES FOR THE EXPERIMENTS

Parameter (Equation #)	MR images	TRUS images
λ_1 (2)	0.05	0.1
λ_2 (2)	0.7	0.1
λ_3 (2)	3	2
α (6)	0.03	0.05

All manual segmentations from our datasets were outlined by a technician and approved by a radiologist with more than ten years experience. The technician providing manual segmentations was excluded in the intra- and inter-observer variability experiments. To avoid users from remembering a previous segmentation, five days were left between resegmentation of the same case in the intra-observer variability test. Two trained graduate students and one trained postdoctoral fellow were involved in the inter-observer variability test. The experimental results were considered significant when the probability of making a type I error was less than 5% ($p < 0.05$) in all statistical analyses.

C. Implementation Details

The proposed algorithm was implemented using parallel computing architecture (CUDA, NVIDIA Corp., Santa Clara, CA, USA) and the user interface in MATLAB (Natick, MA, USA). The GPU based algorithm was developed with nonoptimized MATLAB code based on single-thread programming, which was run in serial on a Windows desktop with an 4-core Intel i7–2600 CPU (3.4 GHz) and a NVIDIA Geforce 5800X GPU. The segmentation time was calculated as the mean run time of five repeated segmentations for each 3-D image. The proposed coherent continuous max-flow computation that is equivalent to the minimization of (6) was parallelized by CUDA and run on the GPU. We also developed a nonoptimized CPU-implemented MATLAB code for the coherent continuous max-flow computation, which has been compared to the GPU-implemented version. For more details, please refer to our public MATLAB source code of the continuous max-flow algorithm, both CPU and GPU versions, are available on the website of MATLAB central[1], which provides useful clues for duplicating the proposed coherent continuous max-flow algorithm. More specifically, the computation of the energy formulations $E(u)$ in (6) including data cost functions $C^{s,t}(x)$ and edge indicator $g(x)$ were developed using serial MATLAB code and run on the CPU, which could be parallelized or converted to C language to speed up the computation. Note that, the MATLAB code for both GPU and CPU version can be better optimized by vectorizing loops, pre-allocating arrays, and using built-in MATLAB functions instead of scripts, etc.

Two parameter sets were used for the TRUS and MR images, respectively, as shown in Table I. The parameters were initially chosen empirically, and then optimized one parameter at a time using five images from the 3T MR images, and five images from 3-D TRUS images, which were chosen randomly from the entire dataset. The DSC [42] was used as the evaluation metric in the

---

[1]http://www.mathworks.com/matlabcentral/fileexchange/34126-fast-continuous-max-flow-algorithm-to-2d3d-image-segmentation
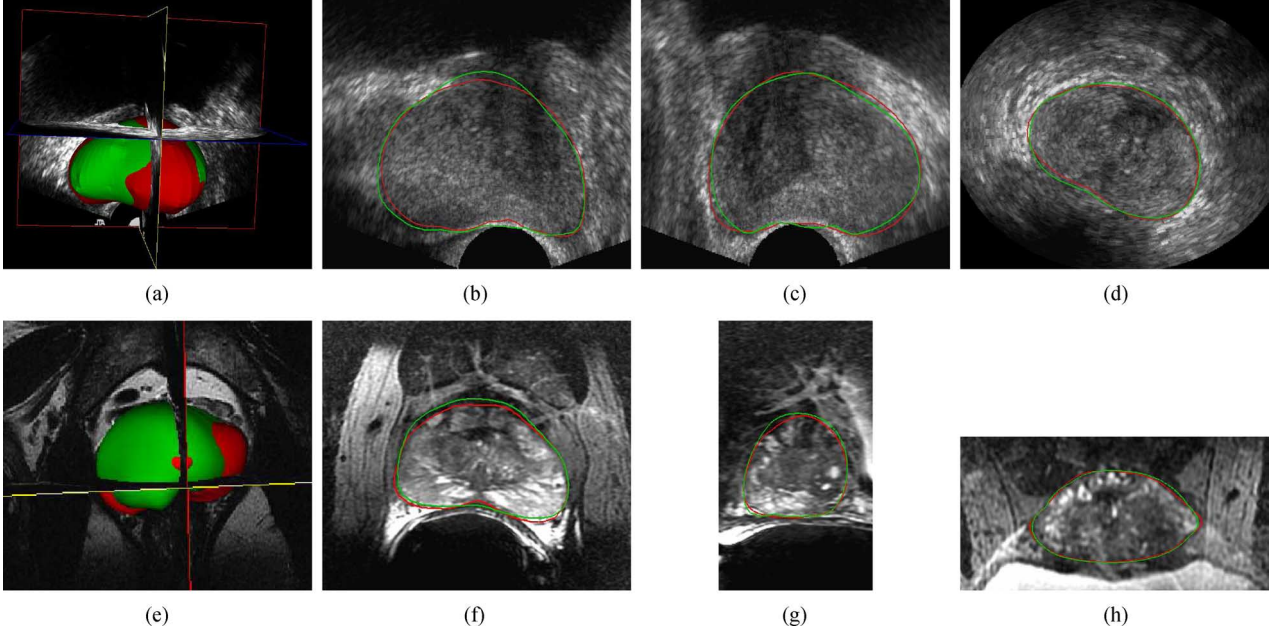
Fig. 5. 3-D prostate segmentation result (green contour) by the proposed method and manual segmentation (red contour). First row: segmentation result using a 3-D TRUS image; second row: segmentation result using a 3-D T2w MR image with an endo-coil. (a), (e) orthogonal view overlapped with the manual segmentation surface; (b), (f) transverse view; (c), (g) sagittal view; (d), (h) coronal view.

TABLE II
SEGMENTATION ACCURACY FOR 25 PATIENT 3-D TRUS IMAGES
(REPRESENTED AS THE MEAN VALUE $\pm$ STANDARD DEVIATION)

	total	base	mid	apex
DSC (%)	93.2 ± 2.0	86.3 ± 3.8	95.1 ± 1.8	87.2 ± 4.8
MAD (mm)	1.1 ± 0.3	0.6 ± 0.4	0.8 ± 0.2	0.7 ± 0.5
MAXD (mm)	3.1 ± 0.6	2.2 ± 0.8	2.8 ± 0.4	2.2 ± 1.0
VD (cm^3)	2.4 ± 1.6	1.4 ± 1.6	1.8 ± 1.0	1.2 ± 1.5

TABLE III
SEGMENTATION ACCURACY FOR 30 PATIENT 3-D
T2w MR IMAGES ACQUIRED IN OUR LABORATORY
(REPRESENTED AS THE MEAN VALUE $\pm$ STANDARD DEVIATION)

	total	base	mid	apex
DSC (%)	88.5 ± 3.5	83.7 ± 4.2	92.6 ± 2.8	84.0 ± 4.0
MAD (mm)	1.8 ± 0.8	2.4 ± 1.6	3.2 ± 2.3	2.1 ± 2.0
MAXD (mm)	8.1 ± 5.5	11.8 ± 11.2	12.2 ± 8.3	13.5 ± 10.0
VD (cm^3)	3.2 ± 1.5	1.2 ± 1.0	1.8 ± 1.2	1.5 ± 1.2

experiments for the choice of the parameters. These parameters were kept constant during the evaluation experiments.

IV. RESULTS

A. Results in 3-D TRUS Images

1) Accuracy: The first row in Fig. 5 shows one example of 3D TRUS prostate segmentation. The validation results using the 25 3-D TRUS images shown in Table II indicate that the proposed method achieved a good segmentation accuracy for the whole prostate gland with a DSC of $93.2\% \pm 2.0\%$, a MAD of 1.1 ± 0.3 mm, a MAXD of 3.1 ± 0.6 mm and a VD of 2.4 ± 1.6 cm^3. More specifically, the proposed yielded the best segmentation accuracy in the middle gland with a DSC of $95.1\% \pm 1.8\%$ and small values of MAD, MAXD, and VD. The accuracy in the regions of apex and base prostate is relatively poorer with higher variations in terms of DSC, MAD, MAXD, and VD, compared to results in the mid-gland.

2) Reproducibility: Three repeated segmentations using the 10 3-D TRUS images randomly selected and initialized by the same observer yielded a mean DSC of 92.7% and a CV of 2.7%, demonstrating a low intra-observer variability. A one-way ANOVA analysis with a single factor ($\alpha = 0.05$) failed to show a statistically significant difference between these three segmentations. Three repetition segmentations using the proposed method on the same dataset initialized

by three other observers yielded a DSC of $93.4\% \pm 2.3\%$, $91.6\% \pm 2.1\%$ and $93.0\% \pm 3.0\%$, and a CV of 2.5%, 2.3%, and 3.2%, respectively. A one-way ANOVA analysis with a single factor ($\alpha = 0.05$) failed to demonstrate a statistically significant difference among these three observers.

3) Computational Time: The mean computational time of the proposed method was determined by five repeated experiments for each 3-D TRUS image. The mean segmentation time acquired by the GPU implemented algorithm was 0.45 ± 0.1 s in addition to about 5 ± 2 s for initialization, resulting in a total processing time of less than 6 s for a given 3-D TRUS prostate image. In contrast, the CPU implemented algorithm required 3 ± 0.5 s in addition to about 5 ± 2 s for initialization, leading to a total processing time of less than 8 s for a given 3-D TRUS prostate image.

B. Results in 3-D MR Images

1) Accuracy in Our In-House Images: The second row in Fig. 5 shows one example of 3D MR prostate segmentation. Table III shows the segmentation results by the proposed method for 30 in-house 3-D MR prostate images. The proposed approach yielded a DSC of $88.5\% \pm 3.5\%$, a MAD of 1.8 ± 0.8 mm, a MAXD of 8.1 ± 5.5 mm, and a VD of 3.2 ± 1.5 cm^3, for the whole prostate gland. The smallest DSC of $83.7\% \pm 4.2\%$ was found at the base region, and the DSC of

TABLE IV
SEGMENTATION ACCURACY FOR 30 PATIENT 3-D MR IMAGES FROM
PUBLIC DATASET OF 2012 MICCAI CHALLENGE (PROMISE12)
(REPRESENTED AS THE MEAN VALUE ± STANDARD DEVIATION)

	total	base	mid	apex
DSC (%)	86.3 ± 4.2	82.7 ± 4.5	91.5 ± 3.1	82.5 ± 4.2
MAD (mm)	2.0 ± 0.9	2.5 ± 1.5	3.5 ± 2.4	2.2 ± 2.0
MAXD (mm)	9.5 ± 5.8	12.5 ± 11.5	13.5 ± 8.2	12.6 ± 10.5
VD (cm^3)	3.5 ± 1.7	1.4 ± 1.2	1.9 ± 1.3	1.8 ± 1.5

TABLE V
PERFORMANCE COMPARISON WITH TWO ROTATIONAL SLICE BASED 3-D
PROSTATE SEGMENTATION METHODS: ACTIVE CONTOUR BASED METHOD
(M_{AC}) AND LEVEL SET BASED METHOD (M_{LS}), USING 10 TRUS AND
15 MR IMAGES IN TERMS OF DSC AND COMPUTATIONAL TIME

	TRUS		MR	
	DSC (%)	Time (s)	DSC (%)	Time (s)
M_{AC}	86.5 ± 4.5	24.5 ± 3.6	-	43.5 ± 3.2
M_{LS}	92.2 ± 3.6	56 ± 3.4	77.5 ± 5.6	75 ± 4.2
$\mathbf{M_{GO}}$	$\mathbf{92.7 \pm 2.7}$	$\mathbf{0.45 \pm 0.1}$	$\mathbf{87.8 \pm 4.6}$	$\mathbf{0.65 \pm 0.15}$

$84.0\% \pm 4.0\%$ for the apex region is relatively small compared to the DSC of $92.6\% \pm 2.8\%$ for the mid region. Details of the MAD, MAXD, and VD results are given in Table III.

2) Accuracy in Public Dataset: Table IV shows the segmentation results by the proposed method for the 30 3-D MR prostate images from a public dataset of the 2012 MICCAI challenge (PROMISE12) [39]. The proposed approach yielded a DSC of $86.3\% \pm 4.2\%$, a MAD of 2.0 ± 0.9 mm, a MAXD of 9.5 ± 5.8 mm, and a VD of 3.5 ± 1.7 cm^3, for the whole prostate gland. The DSCs of $82.7\% \pm 4.5\%$ and $82.5\% \pm 4.2\%$ were found at the base and apex regions, respectively. The largest DSC of $91.5\% \pm 3.1\%$ was obtained for the mid gland region. Details of the MAD, MAXD, and VD results are given in Table IV.

3) Reproducibility: Three repeated segmentations initialized by the same observer on the 15 3-D MR prostate images that were randomly selected yielded a mean DSC of 87.8% and a CV of 4.6%. A one-way ANOVA analysis with a single factor ($\alpha = 0.05$) failed to show a statistically significant difference between these three segmentations, demonstrating a good segmentation consistency for a single observer. Three repetition segmentations initialized by three other observers yielded a DSC of $88.0\% \pm 3.4\%$, $89.2\% \pm 3.8\%$ and $86.5\% \pm 3.6\%$, and a CV of 3.9%, 4.3%, and 4.2%, respectively. The small intra-observer CV of DSC indicates that the algorithm is robust to initializations, and suggests a high reproducibility, independent of the observer. Another one-way ANOVA analysis with a single factor ($\alpha = 0.05$) failed to demonstrate a statistically significant difference between these three observers.

4) Computational Time: The mean segmentation time of the GPU implemented algorithm for one 3-D MR image, calculated using all 3-D MR images, was 0.65 ± 0.15 s, in addition to 4 ± 2 s for initialization, resulting in a total segmentation time of less than 5 s for a given 3-D MR prostate image. In contrast, the CPU implemented algorithm required 5 ± 0.5 s in addition to about 4 ± 2 s for initialization, leading to a total processing time of less than 9 s for a 3-D MR prostate image.

V. DISCUSSION

We described and validated a single novel global optimization based approach for prostate segmentation from both 3-D TRUS and MR images. The proposed approach properly enforces the inherent axial symmetry of prostate shapes to simultaneously adjust a series of 2-D slice-wise segmentations in a "global" 3-D sense. The algorithm provides robust and efficient segmentation results for both 3-D TRUS and MR prostate images. Here, we discuss the algorithm in terms of methodology comparison, accuracy, computational time, and some factors affecting the segmentation accuracy.

A. Comparison With Other Propagation Based Methods

The proposed approach (M_{GO}) was compared to other two rotational slice based 3-D prostate segmentation methods: active contour based method (M_{AC}) [30] and level set based method (M_{LS}) [32], using 10 TRUS and 15 MR images in terms of DSC for the whole prostate gland and segmentation time. In this experiments, the first slice and its initial contour should be carefully determined by the user in order to decrease the associated segmentation errors as much as possible. The comparison of the results shown in Table V indicate that the proposed M_{GO} method achieved the best accuracy result with a mean DSC of 92.7% for 3-D TRUS images and a mean DSC of 87.8% for 3-D MR images. The M_{AC} method yielded the lowest DSC in 3-D TRUS images, and failed to segment most of 3-D MR images with this dataset. The M_{LS} method generated a mean DSC of 92.2% for 3-D TRUS images due to the introduced shape constraint and strong statistical information about the local region, but required more than a factor of 100 in computational time (56 s) than the M_{GO} method (0.45 s) for a given 3-D image. In addition, the M_{LS} method only yielded a mean DSC of 77.5% for 3-D MR images. In contrast, the proposed M_{GO} method yielded a higher mean DSC of 87.8%. A t-test ($\alpha = 0.05$) shows that there is a statistically significant difference between the M_{GO} and M_{LS} methods ($p < 0.005$) in terms of DSC. Table V also reports that the proposed M_{GO} method presented the lowest variability with a standard deviation of 2.7% for the 3-D TRUS images compared to 4.5% of the M_{AC} method and 3.6% of the M_{LS} method. The proposed M_{GO} method also yielded a lower standard deviation of 4.6% for 3-D MR images than 5.6% of the M_{LS} method.

It should be noted that the segmentation accuracy of the M_{AC} and M_{LS} methods relies on the segmentation accuracy of the first slice. Segmentation errors appearing in one slice will be introduced to the segmentation of the next slice and so on, thereby larger errors can accumulate to affect the segmentation of the 3-D TRUS image. In some images, it is challenging to locate the correct prostate boundary based only on the information of a single slice. For examples, when it appears that the overlapped area between the prostate and urethral entrance [the arrow shown in Fig. 6(a)] or seminal vesicle [the arrow shown in Fig. 6(c)] in some TRUS images, it is hard to locate the correct prostate boundary even for radiologists without image information about its neighboring slices. Fig. 6 shows the segmentation results of the M_{AC} and M_{LS} methods with poor initialization for the first slice, illustrated in Fig. 6(a) and (c), respectively. With the result for the first slice, the segmentation accuracy of the M_{AC} method for all slices decreases greatly
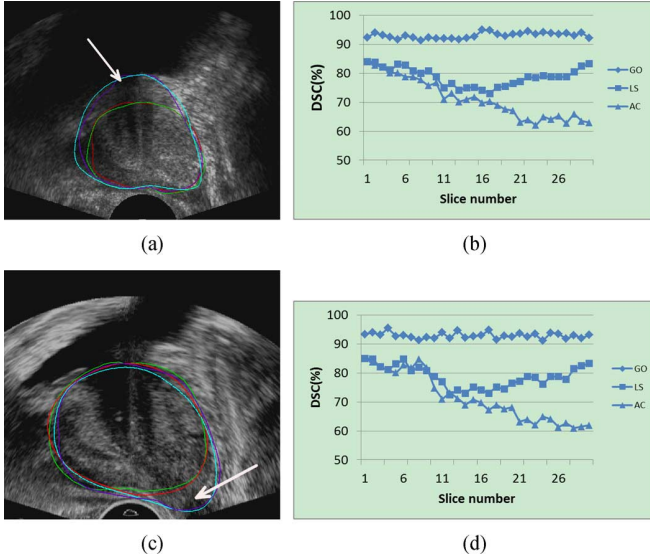
Fig. 6. Comparison results in terms of DSC (%) from two 3-D TRUS image with poor initialization. Green: M_{GO}; red: manual segmentation; blue: M_{LS}; purple: M_{AC}. (a) Segmentation for the first slice containing a urethral region (arrow shows). (b) DSC for all resliced slices based on the segmentation from (a). (c) Segmentation for the first slice containing a seminal vesicle region (arrow shows). (d) DSC for all resliced slices based on the segmentation from (b).

with the progress of the propagation [triangle-patterned curve in Fig. 6(b) and (d)].

The M_{LS} method can decrease the accumulated errors by propagating in two different directions and incorporating some constrains on the evolved level set function, however, its DSC values demonstrate the declining trend in each direction [square-patterned curve in Fig. 6(b) and (d)]. In contrast, the proposed M_{GO} approach performed more reliably with the poor image quality and initialization [diamond-patterned curve in Fig. 6(c) and (d)] compared to the other two methods. Furthermore, we investigated the sensitivity of the methods to a segmentation error in one slice by adding a "bad" segmentation with a DSC of 75% at slice 4 in a 3-D TRUS image. Our results showed that the proposed M_{GO} method still obtained a DSC of 90%, showing that it is insensitive to this disturbance. However, the segmentation accuracy of the M_{AC} and M_{LS} methods decreased from slice 4 onward, and the DSC for slice 15 was only 60% for the M_{AC} method and 70% for the M_{LS} at the end of propagation. These experiments show that the proposed M_{GO} approach is more reliable than the slice-by-slice propagated methods that rely on the segmentation accuracy of the previous slice, since our method makes use of the global rotational correlation between all adjacent slices, which jointly adjusts the segmentation of each slice in a global way, performing more reliably with the poor image quality and initialization compared to the other two methods.

B. Comparison With Other 3-D Prostate Segmentation Methods

It is difficult to compare our results to the results from other state-of-the-art segmentation algorithms due to the differences of the used datasets, manual ground truth, and evaluation metrics. However, we quantitatively compared our proposed approach with prostate segmentation algorithms using 3-D prostate TRUS/MR images, which used similar evaluation metrics.

The quantitative comparison results using 3-D TRUS images in Table VI show that the proposed approach yielded the highest DSC of 93.2% using the shortest computational time compared to other four methods in the literature [11], [18], [45], [46]. A mean MAD of 0.7 ± 0.8 mm and a MAXD of 2.0 ± 1.9 mm obtained by Mahdavi *et al.* [18] are better than our results. However, their results were acquired only in the mid-gland slices instead of the whole prostate gland. Additionally, the method in [18] required user editing after segmentation, increasing the computational time and user interaction. Garnier *et al.* [11] reported a volume overlap rate (VO) of $86.4\% \pm 3.9\%$, a MAD of 0.8 ± 0.3 mm, and a MAXD of 4.8 ± 1.6 mm, which are comparable to our results. But their method required a more complicated initialization and required more computational time.

A direct comparison on the public datasets of 3-D MR images show that the highest mean DSC of $84.3\% \pm 7.1\%$ per image was reported from the MICCAI challenge website [39], which is slightly lower than our results with mean DSC of $86.3\% \pm 4.2\%$. Moreover, it generated a much higher standard deviation of 7.1% in terms of DSC than the proposed method of 4.2%, and required much more computational time of 8 min to segment each image in addition two more hours for training. Compared to this method, the proposed approach demonstrates a great advantage of both computational efficiency and accuracy using the same dataset.

Other quantitative comparison results for 3-D MR images shown in Table VII demonstrate that the proposed method outperformed the methods in [47]–[49] in terms of DSC and computational time. A mean DSC of $88.5\% \pm 3.5\%$ and a MAD of 1.8 ± 0.8 mm obtained by the proposed method are comparable to the results reported in [23], while the proposed method generated a smaller standard deviation of DSC, and reduced the computational time by a factor of 30. It should be noted that the proposed method requires user initialization as an input, which introduces observer variability compared to automatic segmentation techniques. However, the reproducibility evaluation results in Section IV-B show that the inter- and intra- observer variability introduced by user initialization are small.

C. Computational Time

Both GPU- and CPU-implemented algorithms demonstrated great computational performance for both 3-D TRUS and MR images. More specifically, the GPU-implemented algorithm is capable of efficiently segmenting a 3-D TRUS or MR prostate image within 5–6 s compared to 8–9 s required by the CPU-implemented code. However, a great amount of time of 4–5 s was spent on the initialization for both versions. Excluding the time on the initialization, less than 1 s required by the GPU implementation is faster than the CPU implementation by a factor of 6–7. When dealing with the images with larger size or better resolution, the GPU implementation could demonstrate a greater advantage of computation cost. In addition, it typically takes 6–8 s to acquire 3-D TRUS images during the 3-D TRUS guided prostate brachytherapy and biopsy. The developed GPU-implemented algorithm provides a good solution to the prostate

TABLE VI
COMPARISON WITH OTHER PROSTATE SEGMENTATION METHODS ON 3-D TRUS IMAGES (VO IN THE THIRD COLUMN IS VOLUME OVERLAP, DENOTED AS $VO = (V_M \bigcap V_A)/(V_M \bigcup V_A) \times 100$, V_M: MANUAL SEGMENTATION, V_A: ALGORITHMIC SEGMENTATION)

Paper	Year	DSC/VO (%)	MAD (mm)	MAXD (mm)	VD (cm^3)	Time (s)	Type
Tutar[45]	2006	83.5 ± 4.2 (VO)	1.3 ± 0.4	4.1 ± 1.3	-	120	semi-automatic
Garnier[11]	2011	86.4 ± 3.9 (VO)	0.8 ± 0.3	4.8 ± 1.6	-	26	semi-automatic
Mahdavi[18]	2011	-	$\mathbf{0.7 \pm 0.8}$	$\mathbf{2.0 \pm 1.9}$	-	240	semi-automatic
Akbari[46]	2012	90.3 ± 2.3 (DSC)	-	-	-	120-180	automatic
Proposed method	2013	$\mathbf{93.2 \pm 2.0}$ (DSC)	1.1 ± 0.3	3.1 ± 0.6	2.4 ± 1.6	$\mathbf{6}$	semi-automatic

TABLE VII
COMPARISON WITH OTHER PROSTATE SEGMENTATION METHODS ON 3-D MR IMAGES

Paper	Year	DSC (%)	MAD (mm)	MAXD (mm)	VD (cm^3)	Time (s)	Type
Klein[47]	2008	$85.0 - 88.0$	-	-	-	900	automatic
Gao[48]	2010	84.0 ± 3.0	-	8.1 ± 1.5	-	-	automatic
Martin[49]	2010	84	2.4	9.04	-	240	automatic
Toth[23]	2012	88.0 ± 5.0	$\mathbf{1.5 \pm 0.8}$	-	-	150	automatic
Proposed method	2013	$\mathbf{88.5 \pm 3.5}$	1.8 ± 0.8	$\mathbf{8.1 \pm 5.5}$	3.2 ± 1.5	$\mathbf{5}$	semi-automatic

segmentation problem within this time span, which is desired during these interventions. It saves more time for subsequent procedures, such as replanning, dose calculation, and motion compensation.

D. Parameter Sensitivity

All parameters used in this study shown in Table I were kept constant during all evaluation experiments using the 3-D TRUS and MR images. However, the parameter configuration used for most experiments of the in-house and public data may not work well for some images, hence yielding relatively higher segmentation error. For those cases, it was found that tuning parameter values might improve the segmentation accuracy.

1) Symmetry Prior: Axial symmetry as prior prevents the segmented 2-D contours from leaking at locations of weak edges while keeping the spatial consistency between any adjacent 2-D segmented contours. The "soft" constraint $\alpha \subset [0.01, 0.1]$, i.e., the $L1$ penalty, of axial symmetry, in combination with the local image intensity and edge information, is capable of yielding good segmentations if prostate shape deformation caused by tumors, inserted endo-coil, filling bladder, prior treatment undermines the symmetry. A weak symmetry prior ($\alpha < 0.01$) allows more segmentation flexibility only relying on each separate segmentation for each slice, but loses the spatial consistency between any two adjacent contours, leading to a nonsmooth prostate surface. Furthermore, the segmentation for each slice without or with a weak symmetry prior is typically not capable of giving a reliable result due to the presence of speckle, shadowing, and missing edges in TRUS images, and high contrast edges and intensity inhomogeneities in MR images. However, the segmentation with a strong symmetry prior ($\alpha > 0.1$) depends mainly on prior information, ignoring image information, hence gives rise to an identical segmentation contour for each slice.

The effect on the selection of the rotational axis was evaluated by changing the rotational axis. One 3-D TRUS and one MR were randomly chosen in this experiment. Once the initial transverse slice was determined, the rotational axis was manually chosen as a reference. Eight additional rotational axes were also generated by deflecting the rotational axis in the transverse view in two directions with an angle ranging from $-60°$ and
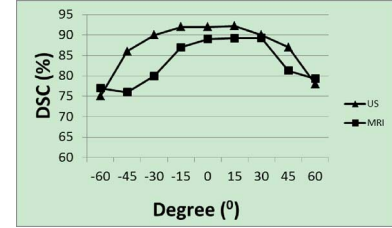

Fig. 7. Plot of DSC versus the deflection angle of the axis of rotation to show the effect on the selection of the rotational axis.
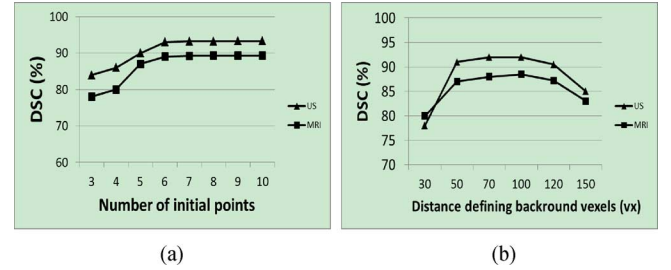

Fig. 8. Results of parameter sensitivity tests in terms of DSC (%). (a) Results of varying the number of user selected points, and (b) results of varying the distance for defining the background voxels.

$60°$. Results in Fig. 7 show that the proposed approach yielded high DSCs when the deflected angle varied from $-30°$ to $30°$, and that the DSC declined when the deflected angle was greater $30°$. We folded the prostate contour in half along the rotational axis in one resliced 2-D image while the deflected angle was $30°$. It was found that the overlap between these two halves was less than 70%, showing a poor symmetry along this axis. When the object is much less symmetrical, e.g., the deflected angle was greater than $30°$, the proposed algorithm failed to give favorable results. Tuning the parameter α of the symmetry prior could improve the accuracy for some particular cases while losing applicability. Thus, the proposed algorithm might not be a good solution to the segmentation of such asymmetrical objects. However, the proposed algorithm could be extended to other applications, such as 3-D vessel or nerve segmentation, by means of reorienting a given 3-D image along the vessel or nerve skeleton
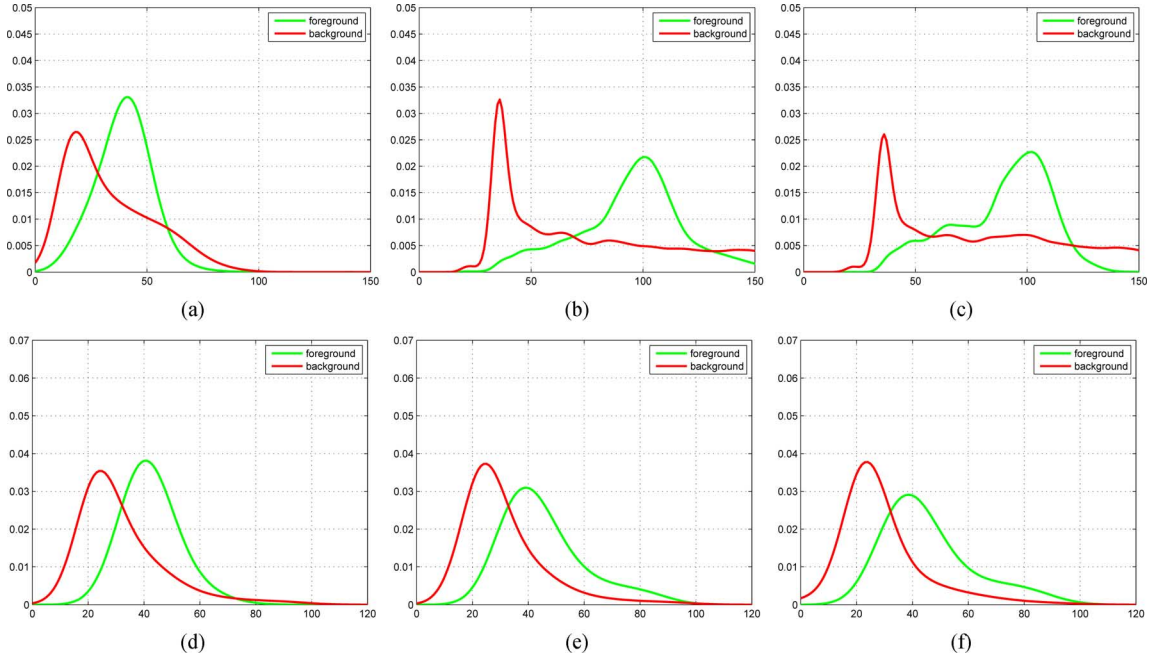
Fig. 9.   Normalized intensity PDF used in 3-D prostate segmentation. Gaussian kernel width of seven was used to generated the PDFs. First row: PDFs for a 3-D TRUS image, second row: PDFs for a 3-D MR image. First column: Model PDFs. Second column: Segmentation result PDFs. Third column: Ground truth PDFs.

and removing the constraint of the left–right horizontal coordinate flipping in (4).

2) Reslicing Step: The resliced step plays an important role influencing the accuracy and efficiency for the slice-by-slice based segmentation methods. The proposed method is slightly sensitive to the parameter of the reslicing step, which is affected by image resolution: a small reslicing step results in a more accurate segmentation, while a large reslicing step leads to a less accurate segmentation, and costs less computational time. The resliced step of $6°$, resulting in a resliced number of slices of 30, is the optimum trade off between efficiency and accuracy, which was appropriate for most of images involved in our in-house TRUS/MR images. But it is large for some 3-D MR prostate images with low resolution from the public MR dataset, leading to a reduced segmentation accuracy of the proposed approach in this dataset (Table IV) compared to the performance result in our in-house MR datasetss (Table III).

3) Number of User Selected Points: The effect of the number of user defined points was investigated in terms of DSC using 10 images, including five 3-D TRUS images and five 3-D MR images. The number of initial points varied from 3 to 10. The results in Fig. 8(a) show that the proposed approach generated similar DSCs when the number of initial points was greater than 6. When the initial points number was smaller than 6, the DSC demonstrates declined. Thus, empirically, the number of initial points used in this application was greater than 6.

4) Distance Defining the Background: During the initialization, voxels outside the fitted contour by a given distance are sampled as the background voxels, which are used to estimate the intensity PDF for the background, and serve as hard constraints of the segmentation regions. We investigated the effect by varying this distance in terms of DSC in 10 images, including five 3-D TRUS images and five 3-D MR images. The results in

Fig. 8(b) show that varying the distance from 50 to 100 voxels is optimal in this study. When the distance was less than 50 voxels, some prostate voxels were mistakenly included in some cases. When the distance was greater than 120 voxels, the sampled background voxels might not well represent the PDF for the background.

5) PDF: The intensity PDF serves as a data cost term to assist the segmentation combined with edge information and a symmetry prior. The experimental images used in this study have different level of noise and inhomogeneity, for example, the dataset from 2012 MICCAI challenge is a representative set of the types of MR images acquired in a clinical setting, which is multi-center and multi-vendor and has different acquisition protocols (i.e., differences in slice thickness, with/without endorectal coil). However, our experimental results demonstrate that the proposed approach is capable of generating a consistently accurate segmentation using these experimental images, suggesting it is insensitive to the PDF profile. Fig. 9 shows the model PDF, final intensity PDFs of the algorithm, and the intensity PDF from manual segmentations for a sample 3-D TRUS and MR image. As can be observed from Fig. 9, although the initial model PDFs are different from the intensity PDFs of the manual segmentations, the final intensity PDFs of the algorithm are very similar to the intensity PDFs from the manual segmentations.

VI. CONCLUSION

In this study, we proposed a novel global optimization approach to the challenging segmenattion of both 3-D prostate TRUS and MR images by enforcing the geometrically axial symmetry of prostate shapes, which coherently segments a series of 2-D reslices under the 'global' perspective. Moreover, we proposed a new *coherent continuous max-flow model*, which

provides a powerful mathematical tool and directly derives a new and efficient duality-based algorithm in numerical practice. Experimental results with different datasets, including 25 3-D TRUS images and 80 3-D T2w MR images with different acquisition protocols from multi-center and multi-vendor, showed that the proposed method can segment the prostate accurately and efficiently from both 3-D TRUS and MR images in terms of DSC, MAD, MAXD, and VD. Another great advantage of the proposed method is that it generated relatively low intra- and inter-observer variability introduced by user manual initialization, suggesting a high reproducibility, independent of the observer. This is useful in multi-center clinical trials where the measurements may be made by multiple observers in different locations at different times. The performance results of our algorithm also suggest that it has the potential to be used for 3-D TRUS/MR image guided prostate interventions. However, in this study, segmentations of 3-D MR and TRUS images for the same patient were separately performed, which failed to take into account the consistency of the same prostate in these two modality images. Co-segmenting two modality images simultaneously, such as using MR images to guide TRUS image segmentation [50], might be a more efficient way to cope with the task of segmenting two modality images for the same patient, which is our future work.

APPENDIX I
PROOF OF PROP. 1

Proof: Introduce the multiplier functions $u_i(x)$, $i = 1 \ldots n$, to the linear equalities (12) and (11), then it is obvious that the *coupled continuous max-flow model* (7) is equivalent the primal-dual model (13), i.e.,

$$(7) \iff (13)$$

which can be easily reorganized as

$$\min_{u_1 \ldots u_n} \max_{p^s, p^t, q, r} \sum_{i=1}^{n} \left\{ \langle p_i^s, 1 - u_i \rangle + \langle p_i^t, u_i \rangle + \langle \operatorname{div} q_i, u_i \rangle \right\}$$
$$+ \int_{\Omega} r_n \left(u_n(L - x_1, x_2) - u_1(x_1, x_2) \right) dx$$
$$+ \sum_{i=1}^{n-1} \langle r_i, u_{i+1} - u_i \rangle \tag{20}$$

subject to the flow constraints (8)–(10).

Observe the minimax theorem by Ekeland and Temam [51], the energy function of (20) is linear in both the flow variables (p^s, p^t, q, r) and the multiplier functions u, and all the constraints on flow variables are convex; therefore, there exists at lease one saddle point of (20) and the min and max operators can be interchanged.

In the following, we prove (20) is equivalent to (6).

Now we consider to first maximize (20) over the flows (p^s, p^t, q, r): let us consider the following maximization problem:

$$f(v) = \max_{w \leq C} w \cdot v \tag{21}$$

where C is a given constant.

When $v < 0$, w can be chosen to be a negative infinity value in order to maximize the value $w \cdot v$, i.e., $f(v) = +\infty$. In consequence, we must have $v \geq 0$ so as to make the function $f(v)$ meaningful. Then

$$\begin{cases} \text{if } v = 0, & \text{then } w \leq C \text{ and } f(v) = 0 \\ \text{if } v > 0, & \text{then } w = C \text{ and } f(v) = v \cdot C \end{cases} . \tag{22}$$

By virtue of (22), we can equally express $f(v)$ by

$$f(v) = v \cdot C, \quad \text{and} \quad v \geq 0. \tag{23}$$

Following the above analysis, the maximization of the first two terms in (20) over the flow p^s and p^t simply gives rise to

$$\sum_{i=1}^{n} \left\{ \langle C_i^s, 1 - u_i \rangle + \langle C_i^t, u_i \rangle \right\}, \quad \text{and } u_i(x) \in [0, 1]. \tag{24}$$

The maximization of the third term in (20) over the spatial flow q [52] gives

$$\sum_{i=1}^{n} \int_{\Omega} g(x) |\nabla u_i| \, dx. \tag{25}$$

Clearly, the maximization of the last two terms in (20) over the coupled flow r results in

$$\int_{\Omega} |u_n(L - x_1, x_2) - u_1(x)| \, dx + \sum_{i=1}^{n-1} \int_{\Omega} |u_{i+1} - u_i| \, dx. \tag{26}$$

In view of (24)–(26), we have

$$(20) \iff (6).$$

Therefore, Prop. 1 is proved.   ∎

APPENDIX II
PROOF OF PROP. 2

Proof: We prove Prop. 2 by means of the proposed *coupled continuous max-flow model*.

Let $(u^*; (p^s)^*, (p^t)^*, (q)^*, r^*)$ be the optimal saddle point of (13) or (20). Clearly, through Prop. 1, the max-flow energy of (7) by $((p^s)^*, (p^t)^*, (q)^*, r^*)$ equals to the minimum energy of (6) by u^*.

Let S_i^γ, $i = 1 \ldots n$, be any upper level-set of $u_i^*(x)$ and $u_i^\gamma(x) \in \{0, 1\}$ be its indicator function.

By virtue of (23), for $\forall x \in \Omega \backslash S_i^\gamma$, $i = 1 \ldots n$, we have $u_i^\gamma(x) \leq \gamma < 1$, i.e., $1 - u_i^\gamma > 0$ and

$$(p_i^s)^*(x) = C_i^s(x)$$

likewise, for $\forall x \in S_i^\gamma$, $i = 1 \ldots n$, we have $u_i^\gamma(x) > \gamma \geq 0$ and

$$(p_i^t)^*(x) = C_i^t(x).$$

Moreover, the optimum flows $((p^s)^*, (p^t)^*, (q)^*, r^*)$ satisfy the flow conservation conditions (11) and (12), such that

$$\left(\operatorname{div}(q_i)^* - (p_i^s)^* + (p_i^t)^* + (r_i)^* - (r_{i-1})^* \right)(x) = 0$$

for $i = 1 \ldots n - 1$, and

$$\left(\operatorname{div}(q_1)^* - (p_1^s)^* + (p_1^t)^* + (r_1)^* \right)(x) - (r_n)^*(L - x_1, x_2) = 0.$$

Hence, for $x \in S_i^\gamma$, $i = 1 \ldots n$, we have

$$(p_i^s)^*(x) = \big(\operatorname{div}(q_i)^* + (p_i^t)^* + (r_i)^* - (r_{i-1})^* \big)(x)$$

for $i = 1 \ldots n - 1$, and

$$(p_1^s)^*(x) = \big(\operatorname{div}(q_1)^* + (p_1^t)^* + (r_1)^* \big)(x) - (r_n)^*(L - x_1, x_2).$$

Therefore, we compute the maximum flow energy

$$\sum_{i=1}^n \int_\Omega (p_i^s)^* \, dx$$

and consider that thresholding does not change the sign, i.e., $u_{i+1}^\gamma(x) - u_i^\gamma(x)$ has the same sign of $u_{i+1}^*(x) - u_i^*(x)$ for $x \in \Omega$, which finally results in

$$\sum_{i=1}^n E_i(u_i^\gamma) + \alpha \sum_{i=1}^n \pi_i(u^\gamma). \tag{27}$$

On the other hand, the maximum flow energy also equals to the minimum energy of

$$\sum_{i=1}^n E_i(u_i^*) + \alpha \sum_{i=1}^n \pi_i(u^*) \tag{28}$$

which gives the global minimum energy.

Therefore, the energy of (27) also gives the global minimum energy, then the functions $u_i^\gamma(x) \in \{0, 1\}$, $i = 1 \ldots n$, solve the combinatorial optimization problem (5) globally!

Prop. 2 is proved. ∎

REFERENCES

[1] S. Natarajan, L. S. Marks, D. J. Margolis, J. Huang, M. L. Macairan, P. Lieu, and A. Fenster, "Clinical application of a 3-D ultrasound-guided prostate biopsy system," *Urologic Oncol.: Seminars Original Investigat.*, vol. 29, no. 3, pp. 334–342, 2011.

[2] P. A. Pinto *et al.*, "Magnetic resonance imaging/ultrasound fusion guided prostate biopsy improves cancer detection following transrectal ultrasound biopsy and correlates with multiparametric magnetic resonance imaging," *J. Urol.*, vol. 186, no. 4, pp. 1281–1285, 2011.

[3] S. Leslie, A. Goh, P.-M. Lewandowski, E. Y.-H. Huang, A. L. de Castro Abreu, A. K. Berger, H. Ahmadi, I. Jayaratna, S. Shoji, I. S. Gill, and O. Ukimura, "2050 contemporary image-guided targeted prostate biopsy better characterizes cancer volume, Gleason grade and its 3-D location compared to systematic biopsy," *J. Urol.*, vol. 187, no. 4, p. e827, 2012.

[4] A. Krieger, R. Susil, C. Menard, J. Coleman, G. Fichtinger, E. Atalar, and L. Whitcomb, "Design of a novel MRI compatible manipulator for image guided prostate interventions," *IEEE Trans. Biomed. Eng.*, vol. 52, no. 2, pp. 306–313, Feb. 2005.

[5] Y. Zhu, S. Williams, and R. Zwiggelaar, "Computer technology in detection and staging of prostate carcinoma: A review," *Med. Image Anal.*, vol. 10, no. 2, pp. 178–199, 2006.

[6] V. V. Karnik, A. Fenster, J. Bax, D. W. Cool, L. Gardi, I. Gyacskov, C. Romagnoli, and A. D. Ward, "Assessment of image registration accuracy in three-dimensional transrectal ultrasound guided prostate biopsy," *Med. Phys.*, vol. 37, no. 2, pp. 802–813, Feb. 2010.

[7] V. V. Karnik, A. Fenster, J. Bax, C. Romagnoli, and A. D. Ward, "Evaluation of intersession 3-D-TRUS to 3-D-TRUS image registration for repeat prostate biopsies," *Med. Phys.*, vol. 38, no. 4, pp. 1832–1843, Apr. 2011.

[8] R. Kirby and P. Gilling, *Fast Facts: Benign Prostatic Hyperplasia*. Oxfordshire , U.K.: Health Press, 2011.

[9] N. D. Nanayakkara, J. Samarabandu, and A. Fenster, "Prostate segmentation by feature enhancement using domain knowledge and adaptive region based operations," *Phys. Med. Biol.*, vol. 51, no. 7, pp. 1831–1848, Apr. 2006.

[10] Z. Wei, G. Wan, L. Gardi, G. Mills, D. Downey, and A. Fenster, "Robot-assisted 3-D-TRUS guided prostate brachytherapy: System integration and validation," *Med. Phys.*, vol. 31, no. 3, pp. 539–548, Mar. 2004.

[11] C. Garnier, J.-J. Bellanger, K. Wu, H. Shu, N. Costet, R. Mathieu, R. de Crevoisier, and J.-L. Coatrieux, "Prostate segmentation in HIFU therapy," *IEEE Trans. Med. Imag.*, vol. 30, no. 3, pp. 792–803, Mar. 2011.

[12] V. Chalasani, L. Gardi, C. H. Martinez, D. B. Downey, A. Fenster, and J. L. Chin, "Contemporary technique of intraoperative 3-dimensional ultrasonography-guided transperineal prostate cryotherapy," *Can. Urol. Assoc. J.*, vol. 3, no. 2, pp. 136–141, 2009.

[13] C. Zini, E. Hipp, S. Thomas, A. Napoli, C. Catalano, and A. Oto, "Ultrasound- and MR-guided focused ultrasound surgery for prostate cancer," *World J. Radiol.*, vol. 4, no. 6, pp. 247–252, 2012.

[14] A. Sciarra, J. Barentsz, A. Bjartell, J. Eastham, H. Hricak, V. Panebianco, and J. A. Witjes, "Advances in magnetic resonance imaging: How they are changing the management of prostate cancer," *Eur. Urol.*, vol. 59, no. 6, pp. 962–977, Jun. 2011.

[15] B. Fei, D. M. Schuster, V. Master, H. Akbari, A. Fenster, and P. Nieh, "A molecular image-directed 3-D ultrasound-guided biopsy system for the prostate," in *Proc. SPIE Med. Imag.*, 2012, pp. 831 613–831 613.

[16] Y. Zhan, D. Shen, J. Zeng, L. Sun, G. Fichtinger, J. Moul, and C. Davatzikos, "Targeted prostate biopsy using statistical image analysis," *IEEE Trans. Med. Imag.*, vol. 26, no. 6, pp. 779–788, Jun. 2007.

[17] Y. Zhan and D. Shen, "Deformable segmentation of 3-D ultrasound prostate images using statistical texture matching method," *IEEE Trans. Med. Imag.*, vol. 25, no. 3, pp. 256–272, Mar. 2006.

[18] S. S. Mahdavi, M. Moradi, X. Wen, W. J. Morris, and S. E. Salcudean, "Evaluation of visualization of the prostate gland in vibro-elastography images," *Med. Image Anal.*, vol. 15, no. 4, pp. 589–600, 2011.

[19] H. Akbari, X. Yang, L. V. Halig, and B. Fei, "3-D segmentation of prostate ultrasound images using wavelet transform," in *Proc. SPIE Med. Imag.*, 2011, pp. 79 622K–79 622K.

[20] X. Yang and B. Fei, "3-D prostate segmentation of ultrasound images combining longitudinal image registration and machine learning," in *Proc. SPIE Med. Imag.*, 2012, pp. 83 162O–83 162O.

[21] H. Akbari and B. Fei, "3-D ultrasound image segmentation using wavelet support vector machines," *Med. Phys.*, vol. 39, no. 6, pp. 2972–2984, 2012.

[22] S. Chandra, J. Dowling, K.-K. Shen, P. Raniga, J. P. W. Pluim, P. Greer, O. Salvado, and J. Fripp, "Patient specific prostate segmentation in 3-d magnetic resonance images," *IEEE Trans. Med. Imag.*, vol. 31, no. 10, pp. 1955–1964, Oct. 2012.

[23] R. Toth and A. Madabhushi, "Multifeature landmark-free active appearance models: Application to prostate MRI segmentation," *IEEE Trans. Med. Imag.*, vol. 31, no. 8, pp. 1638–1650, Aug. 2012.

[24] J. A. Noble and D. Boukerroui, "Ultrasound image segmentation: A survey," *IEEE Trans. Med. Imag.*, vol. 25, no. 8, pp. 987–1010, Aug. 2006.

[25] Y. Zhu, S. Williams, and R. Zwiggelaar, "Computer technology in detection and staging of prostate carcinoma: A review," *Med. Image Anal.*, vol. 10, no. 2, pp. 178–199, Apr. 2006.

[26] S. Ghose, A. Oliver, R. Martí, X. Lladó, J. Vilanova, J. Freixenet, J. Mitra, D. Sidibé, and F. Meriaudeau, "A survey of prostate segmentation methodologies in ultrasound, magnetic resonance and computed tomography images," *Comput. Methods Programs Biomed.*, vol. 108, no. 1, pp. 262–287, 2012.

[27] T. Heimann and H.-P. Meinzer, "Statistical shape models for 3-D medical image segmentation: A review," *Med. Image Anal.*, vol. 13, no. 4, pp. 543–563, 2009.

[28] R. Toth, P. Tiwari, M. Rosen, G. Reed, J. Kurhanewicz, A. Kalyanpur, S. Pungavkar, and A. Madabhushi, "A magnetic resonance spectroscopy driven initialization scheme for active shape model based prostate segmentation," *Med. Image Anal.*, vol. 15, no. 2, pp. 214–225, 2011.

[29] J. Yuan, W. Qiu, E. Ukwatta, M. Rajchl, Y. Sun, and A. Fenster, "An efficient convex optimization approach to 3-D prostate MRI segmentation with generic star shape prior," in *MICCAI Prostate MR Image Segmentat. Challenge*, 2012.

[30] M. Ding, H. N. Cardinal, and A. Fenster, "Automatic needle segmentation in three-dimensional ultrasound images using two orthogonal two-dimensional image projections," *Med. Phys.*, vol. 30, no. 2, pp. 222–234, Feb. 2003.

[31] W. Qiu, J. Yuan, E. Ukwatta, D. Tessier, and A. Fenster, "Rotational-slice-based prostate segmentation using level set with shape constraint for 3-D end-firing TRUS guided biopsy," in *Proc. MICCAI*, 2012, vol. 7510, pp. 536–543.

[32] W. Qiu, J. Yuan, E. Ukwatta, D. Tessier, and A. Fenster, "3-D prostate segmentation using level set with shape constraint based on rotational slices for 3-D end-firing TRUS guided biopsy," *Med. Phy.*, vol. 40, no. 7, 2013.

[33] J. Yuan, W. Qiu, E. Ukwatta, M. Rajchl, X. Tai, and A. Fenster, "Efficient 3-D endfiring TRUS prostate segmentation with globally optimized rotational symmetry," in *Proc. IEEE Conf. Comput. Vis. Pattern Recognit.*, Jun. 2013, pp. 2211–2218.

[34] T. F. Chan, S. Esedoglu, and M. Nikolova, "Algorithms for finding global minimizers of image segmentation and denoising models," *SIAM J. Appl. Math.*, vol. 66, no. 5, pp. 1632–1648, 2006.

[35] J. Yuan, E. Bae, and X. Tai, "A study on continuous max-flow and min-cut approaches," in *Proc. Comput. Vis. Pattern Recognit.*, 2010.

[36] D. P. Bertsekas, *Nonlinear Programming*. Nashua, NH: Athena Scientific, 1999.

[37] R. T. Rockafellar, "Augmented Lagrangians and applications of the proximal point algorithm in convex programming," *Math. Oper. Res.*, vol. 1, no. 2, pp. 97–116, 1976.

[38] A. Chambolle, "An algorithm for total variation minimization and applications," *J. Math. Imag. Vis.*, vol. 20, no. 1, pp. 89–97, Jan. 2004.

[39] Grand challenge: Prostate MR image segmentation Oct. 2012 [Online]. Available: http://promise12.grand-challenge.org/

[40] J. Bax, D. Cool, L. Gardi, K. Knight, D. Smith, J. Montreuil, S. Sherebrin, C. Romagnoli, and A. Fenster, "Mechanically assisted 3-D ultrasound guided prostate biopsy system," *Med. Phys.*, vol. 35, no. 12, pp. 5397–5410, 2008.

[41] Automated segmentation of prostate structures NCI-ISBI, Apr. 2013 [Online]. Available: https://wiki.cancerimagingarchive.net/display/Public/NCI-ISBI+2013+Challenge+-+Automated+Segmentation+of+Prostate+Structures

[42] K. Zou, S. Warfield, A. Bharatha, C. Tempany, M. Kaus, S. Haker, W. Wells, F. Jolesz, and R. Kikinis, "Statistical validation of image segmentation quality based on a spatial overlap index," *Acad. Radiol.*, vol. 11, no. 2, pp. 178–189, 2004.

[43] M. Ding, B. Chiu, I. Gyacskov, X. Yuan, M. Drangova, D. B. Downey, and A. Fenster, "Fast prostate segmentation in 3-D TRUS images based on continuity constraint using an autoregressive model," *Med. Phys.*, vol. 34, no. 11, pp. 4109–4125, 2007.

[44] K. H. Zou and M. P. Mcdermott, "Higher-moment approaches to approximate interval estimation for a certain intraclass correlation coefficient," *Stat. Med.*, vol. 18, no. 15, pp. 2051–2061, 1999.

[45] I. B. Tutar, S. D. Pathak, L. Gong, P. S. Cho, K. Wallner, and Y. Kim, "Semiautomatic 3-D prostate segmentation from TRUS images using spherical harmonics," *IEEE Trans. Med. Imag.*, vol. 25, no. 12, pp. 1645–1654, Dec. 2006.

[46] H. Akbari and B. Fei, "3-D ultrasound image segmentation using wavelet support vector machines," *Med. Phys.*, vol. 39, no. 6, pp. 2972–2984, 2012.

[47] S. Klein, U. A. van der Heide, I. M. Lips, M. van Vulpen, M. Staring, and J. P. Pluim, "Automatic segmentation of the prostate in 3-D MR images by atlas matching using localized mutual information," *Med. Phys.*, vol. 35, pp. 1407–1418, 2008.

[48] Y. Gao, R. Sandhu, G. Fichtinger, and A. Tannenbaum, "A coupled global registration and segmentation framework with application to magnetic resonance prostate imagery," *IEEE Trans. Med. Imag.*, vol. 29, no. 10, pp. 1781–1794, Oct. 2010.

[49] S. Martin, J. Troccaz, and V. Daanen, "Automated segmentation of the prostate in 3-D MR images using a probabilistic atlas and a spatially constrained deformable model," *Med. Phys.*, vol. 37, p. 1579, 2010.

[50] Y. Hu, T. J. Carter, H. U. Ahmed, M. Emberton, C. Allen, D. J. Hawkes, and D. C. Barratt, "Modelling prostate motion for data fusion during image-guided interventions," *IEEE Trans. Med. Imag.*, vol. 30, no. 11, pp. 1887–1900, Nov. 2011.

[51] I. Ekeland and R. Temam, *Convex Analysis and Variational Problems*. Philadelphia, PA: SIAM, 1999.

[52] E. Giusti, *Minimal Surfaces and Functions of Bounded Variation*. Berlin, Germany: Birkhauser, 1984, vol. 80.